RSC Advances

PAPER

View Article Online
View Journal | View Issue

Cite this: *RSC Adv.*, 2019, **9**, 32247

A N-doped graphene–cobalt nickel sulfide aerogel as a sulfur host for lithium–sulfur batteries†

Ping Wu,[a] Hai-Yan Hu,[a] Ning Xie,[b] Chen Wang,[a] Fan Wu,[a] Ming Pan,[a] Hua-Fei Li,[b] Xiao-Di Wang,[a] Zheling Zeng,[a] Shuguang Deng *[c] and Gui-Ping Dai *[a]

Received 9th July 2019
Accepted 24th September 2019

DOI: 10.1039/c9ra05202j

rsc.li/rsc-advances

Herein, three-dimensional (3D) N-doped reduced graphene oxide (N-rGO) nanosheets were decorated with a uniform distribution of Co–Ni–S (CNS) nanoparticles to form the CNS/N-rGO composite as a sulfur host material for lithium–sulfur batteries. The CNS nanoparticles and N in CNS/N-rGO strongly interact with polysulfides, whereas graphene, as a conductive network, can improve its electrical conductivity. A CNS/N-rGO/sulfur composite cathode was prepared *via* the sulfur melting diffusion method. The electrochemical study showed that the CNS/N-rGO/sulfur cathode delivered an initial discharge capacity of 1430 mA h g^{-1} at a current density of 0.1C. Moreover, it retained a specific capacity of 685 mA h g^{-1} after 300 cycles at 0.5C with a coulombic efficiency of 98%, which was better than that of commercial rGO. This composite was used as a sulfur cathode for a lithium–sulfur battery, exhibiting excellent rate capability and remarkable performance in terms of long cycling stability.

1. Introduction

Due to the increasing energy density requirements of lithium-ion secondary batteries for electric vehicles and portable electronic devices in recent years,[1,2] conventional lithium-ion batteries cannot satisfy the high capacity requirements of batteries due to their low energy density. Thus, lithium–sulfur (Li–S) batteries using elemental sulfur as a cathode material have attracted extensive attention due to their high theoretical specific capacity and theoretical energy density of 1675 mA h g^{-1} and 2600 W h kg^{-1}, respectively, which is much higher than that of commercial cobalt acid lithium batteries (<150 mA h g^{-1}).[3] In addition, elemental sulfur is abundant on Earth, and it is an environmentally friendly element that causes a weak pollution to the environment.[4] Therefore, Li–S batteries are considered as one of the most promising high energy density secondary batteries in the next generation.[5,6]

However, the development of lithium–sulfur batteries is still hampered by many challenges, which mainly stem from the sulfur cathode.[7] The first main issue is that the inherent electronic insulation of elemental sulfur and its discharge final product, Li_2S_2/Li_2S, limit the utilization of active materials and the high rate performance of batteries.[7,8] The second major problem is the shuttle effect, which results in performance degradation of the Li–S batteries. On the one hand, soluble lithium polysulfide intermediates (LiPSs, Li_2S_x, $4 \leq x \leq 8$) are produced during the charge–discharge process, which increase the viscosity of the electrolyte and decrease the conductivity of the ions.[9–11] Moreover, due to the concentration gradient, LiPSs can diffuse through the separator to the anode and deposit the insoluble Li_2S_2/Li_2S on the Li anode surface, which destroys the solid electrolyte interface (SEI) layer on the anode surface, resulting in the rapid deterioration of the battery capacity.[1,12–14] On the other hand, LiPSs shuttle back and forth between the cathode and anode, leading to severe overcharging of the battery during the charging process and diminishing the coulombic efficiency.[15–17] In addition, the shuttles cause a corrosive reaction on the surface of metallic lithium.[1,8] The third issue arises from the difference in the density of sulfur and its discharge products, resulting in about 80% volume change during the charge–discharge process; this causes sulfur to easily detach from the conductive skeleton network and powdering of the cathode, resulting in the failure of the battery.[18–20]

Thus, to address the abovementioned challenges, researchers have attempted to study the modification of composite cathode materials, focusing on improving the conductivity and stability of sulfur-based cathode materials, inhibiting sulfur loss in the active components, and preventing the dissolution of polysulfides in the electrolyte.[17] Recently, carbon matrices have been widely used to form composites with sulfur, such as porous carbon,[15,19,21,22] carbon fibers,[10,23,24] carbon nanotubes,[9,25–27] and graphene.[28–32] Manthiram and

[a]*Department of Chemical Engineering, School of Environmental and Chemical Engineering, Nanchang University, Nanchang 330031, Jiangxi, China. E-mail: nanodai@gmail.com*

[b]*Institute for Advanced Study, Nanchang University, Nanchang, Jiangxi 330031, China*

[c]*Department of Chemical Engineering, School for Engineering of Matter Transport and Energy, Arizona State University, Tempe, AZ 85287, USA. E-mail: Shuguang.Deng@asu.edu*

† Electronic supplementary information (ESI) available. See DOI: 10.1039/c9ra05202j

coworkers designed a freestanding, three-dimensional graphene/1T MoS_2 (3DG/TM) heterostructure with highly efficient electrocatalysis properties for lithium polysulfides (LiPSs) due to excellent ion/electron transfer and the presence of sufficient electrocatalytic active sites. Consequently, the cells with 3DG/TM exhibited an outstanding electrochemical performance, with a high reversible discharge capacity of 1181 mA h g^{-1} and a capacity retention of 96.3% after 200 cycles.[33] Zhang and coworkers presented a radical-directed, lithium-compatible, and strongly polysulfide-solvating high-dielectric electrolyte based on tetramethylurea. Over 200 h of cycling was realized in Li|Li symmetric cells, and it enabled pouch cells to deliver a discharge capacity of 1524 mA h g^{-1} and an energy density of 324 W h kg^{-1}.[34] Li and coworkers used a facile spray-drying method to design a unique three-dimensional hierarchical microsphere architecture assembled by oxygen-deficient $La(OH)_3$ and reduced graphene oxide (rGO) as a sulfur host material for Li–S batteries. The sulfur cathode with rGO–$La(OH)_3$ exhibited a high initial specific capacity of 1160.4 mA h g^{-1} at 0.2C and retained long-term stability with a capacity of 541.7 mA h g^{-1} after 600 cycles at 1C.[35] Among the carbon materials, graphene and its derivatives have been considered as one of the most promising carbon materials for improving the Li–S battery system because of their excellent electronic conductivity and high specific surface area.[36–38] However, pure graphene has relatively stable chemical properties, and thus it cannot interact with the active material of the Li–S batteries, resulting in poor ability to alleviate the "shuttle effect" of polysulfides. In fact, there are two factors that determine the performance of cathode materials, one is the structural factor, and the other is the catalytic factor.[39] Therefore, it is necessary to modify the surface functional groups of graphene by doping heteroatoms (N, O, and S)[40–42] or combining it with metal compounds (Fe_2O_3 and CoS_2).[43,44] Qiu *et al.*[45] reported the preparation of nitrogen-doped graphene (NG)/sulfur composites with high conductivity *via* the thermal nitridation of graphene oxide with ammonia. They found that the graphene-doped pyridinic N and pyrrolic N could form $S_xLi\cdots N$ with polysulfides, thus alleviating the dissolution of polysulfides. Simultaneously, they also found that the strong interaction between NG and polysulfides is the main cause of the ionic attraction between N and lithium ions, rather than the interaction between N and sulfur ions. In addition, transition metal sulfides can also interact strongly with polysulfides. For example, CoS_2 and NiS_2 have been attracting increasing attention recently because of their unique metallic conductivity.[46] Yuan *et al.*[44] reported that upon the introduction of CoS_2 in the carbon/sulfur cathode, due to the strong interaction between CoS_2 and lithium polysulfides, CoS_2 can adsorb polar polysulfides and offer activation sites, which accelerates the polysulfides redox reaction and prolongs the cycle life of Li–S batteries. Lu *et al.*[47] reported that the strong interaction between CoS_2 and polysulfides and NiS_2 can promote the redox kinetics of polysulfides and both of them can improve the conductivity of Li–S battery electrode materials. However, these measures still have shortcomings, such as low coulombic efficiency and limited cycle life. Therefore, herein to make better use of the excellent performance of CoS_2 and NiS_2 in Li–S batteries, we combined CoS_2 and NiS_2 to prepare bimetallic sulfides, which may show better electrochemical performances,[48,49] and to solve the shuttle effect problem, an N and metal sulfide co-doped graphene composite was designed and synthesized to improve the performance of Li–S batteries. Subsequently, the composite material was used for the electrocatalysis of the oxygen evolution reaction (OER) and oxygen reduction reaction (ORR).[50,51] The application of this composite in Li–S batteries has not been reported to date.

In this work, we first proposed the one-step hydrothermal synthesis of a Co–Ni–S (CNS) and N co-doped three-dimensional (3D) reduced graphene oxide (CNS/N-rGO) composite as a sulfur host material. The 3D network structure of graphene can provide void spaces for the accommodation of sulfur and facilitate the transmission of ions and electrons. Sulfur was impregnated into this composite *via* the sulfur melting diffusion method, affording a composite containing 72.8 wt% sulfur. The overall process is illustrated in Fig. 1. This CNS/N-rGO composite delivered a high specific capacity of 1430 mA h g^{-1} at the initial discharge of 0.1C, and it maintained a specific capacity of 526 mA h g^{-1} after 500 cycles at 1C, which demonstrate its excellent electrochemical performance as a cathode material for Li–S batteries. All specific capacity values were obtained based on the mass of elemental sulfur.

2. Results and discussion

2.1. Structure and morphology characterization

The surface microstructure characterization of CNS/N-rGO and CNS/N-rGO/S was obtained by SEM observation (please check experimental details in ESI†). As can be seen from Fig. 2a, CNS/N-rGO exhibits a 3D network structure with highly interconnected channels. Moreover, the typical wrinkled and corrugated layered structures are shown in the SEM image (Fig. 2b) at high magnification, and Co–Ni–S (CNS) nanoparticles uniformly distributed in the rGO layer can be observed. The flexible porous structure of rGO promotes the contact between the electrolyte and sulfur, and facilitates the transfer of electrons and ions.[52] Fig. 2c shows that CNS/N-rGO/S composite is still a three-dimensional interconnected porous structure with no sulfur aggregation on its surface, indicating that sulfur is encapsulated by the CNS/N-rGO sheets. The TGA curve in Fig. 2d demonstrates that the sulfur content in the CNS/N-rGO/S composite prepared by melting diffusion is 72.8%. Furthermore, from the TG analysis of CNS/N-rGO, there is almost no mass loss until the temperature reached 450 °C, and the weight of CNS/N-rGO decreased from about 450 °C to 800 °C, which is due to the degradation of CoS_2 and NiS_2 between 450 °C and 800 °C. Therefore, it can be concluded that the contents of CoS_2 and NiS_2 in CNS/N-rGO account for about 7%, while the rest is N-rGO.

The structural features of the CNS/N-rGO and CNS/N-rGO/S composites were characterized *via* BET, XRD and Raman spectroscopy, as shown in Fig. 3. The N_2 adsorption–desorption isotherms together with the BJH pore size distributions of the materials are shown in Fig. 3a and b, respectively. The isotherms

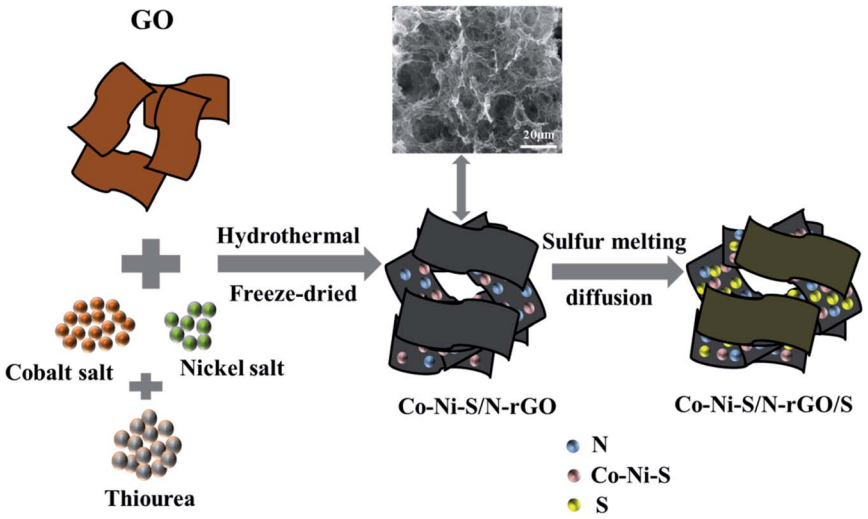

Fig. 1 Schematic of the preparation procedure for the CNS/N-rGO/S composite.

of CNS/N-rGO and CNS/N-rGO/S present typical type-IV isotherms with a significant hysteresis loop, suggesting the existence of a mesoporous structure in the materials. In addition, the CNS/N-rGO possesses a BET specific surface area of 177 $m^2\ g^{-1}$ and cumulative pore volume of 0.416 $cm^3\ g^{-1}$, while that of CNS/N-rGO/S are only 18 $m^2\ g^{-1}$ and 0.09 $cm^3\ g^{-1}$, respectively. Fig. 3b shows the pore size distributions obtained by the BJH desorption isotherm, in which CNS/N-rGO has two mesoporous peaks at 2.8 and 4 nm, while the peak intensity of CNS/N-rGO/S at 4 nm is obviously weaker than that of the sulfur host CNS/N-rGO. It is clearly shown that sulfur is filled in the channels and pores of CNS/N-rGO, which demonstrates the strong interaction between sulfur and the CNS/N-rGO network.[53] Furthermore, the mesoporous structure can provide tunnels for the transport of Li ions and is beneficial to enhance the utilization of S.[7,39] The X-ray diffraction (XRD) patterns of CNS/N-rGO, CNS/N-rGO/S and

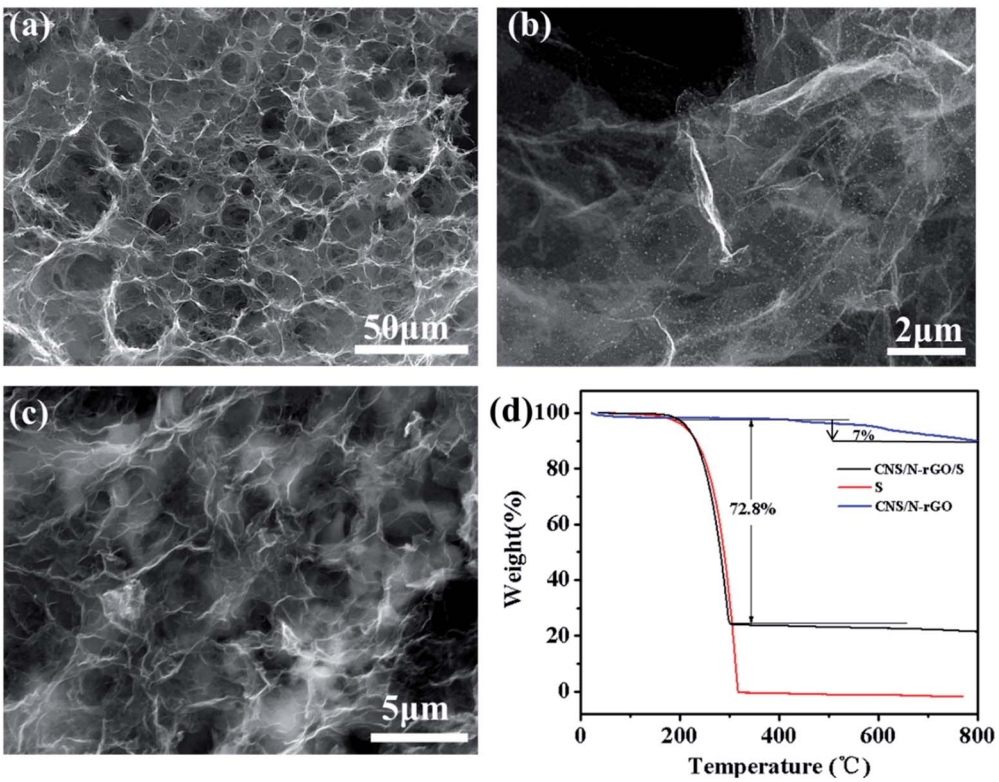

Fig. 2 SEM images of CNS/N-rGO at (a) low and (b) high magnification and (c) CNS/N-rGO/S composite. (d) TGA curves of the CNS/N-rGO/S composite, pure sulfur and CNS/N-rGO composite from room temperature to 800 °C under N_2.

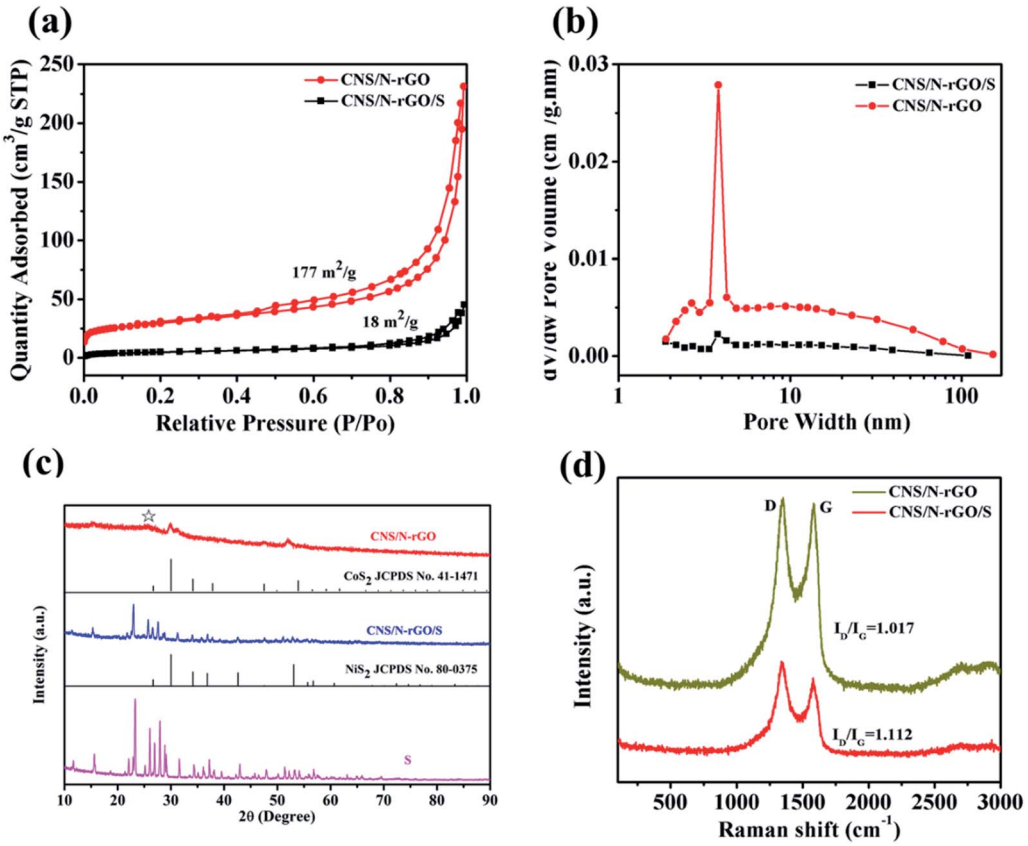

Fig. 3 (a) Nitrogen adsorption–desorption isotherms and (b) BJH pore size distribution plots of CNS/N-rGO and CNS/N-rGO/S. (c) XRD patterns of CNS/N-rGO, CNS/N-rGO/S and S. (d) Raman spectra of CNS/N-rGO and CNS/N-rGO/S.

pure sulfur are shown in Fig. 3c. Compared with pure sulfur, it can be observed that there is no apparent difference in the position of the diffraction peaks in CNS/N-rGO/S, but the intensity of the diffraction peaks of crystalline sulfur is lower. The broad peak for CNS/N-rGO at 26° is attributed to the diffraction of the (002) graphite layered structure. The characteristic peaks at 32.01°, 49.03° and 53.04° correspond to the (200), (220) and (311) planes of CoS_2 (JCPDS no. 41-1471) and NiS_2 (JCPDS no. 80-0375),[54] indicating that the formed CNS nanoparticles are composed of CoS_2 and NiS_2, which could be proven by XPS. According to the Raman spectra in Fig. 3d, the D peak observed at about 1350 cm^{-1} can be ascribed to the structural defects of graphene, and the G peak observed at 1580 cm^{-1} reflects the stretching mode of the C–C bonds of graphene.[55] It can be observed that CNS/N-rGO/S (1.112) has a higher I_D/I_G intensity ratio than that of CNS/N-rGO (1.017) due to the greater amount of defect sites caused by sulfur entering the graphene nanosheets. The addition of sulfur increases the defects of the composite probably because the grinding process of sulfur loading and the heat treatment process during sulfur melting diffusion changed the structure of graphene.

The chemical valence states of Co, Ni, S and N in CNS/N-rGO were further characterized by XPS (Fig. 4). The Co 2p spectrum was deconvoluted into six peaks, which are shown in Fig. 4a, including pairs of fitting peaks of Co^{2+} (781.0 and 797.0 eV) and Co^{3+} (778.2 and 793.4 eV), and satellite peaks at 785.9 and 803.2 eV.[56] It can be seen that the peak area of Co^{2+} is much larger than that of Co^{3+} (Co^{2+}/Co^{3+} = 6.73/1), indicating cobalt basically exists in the form of the +2 state. In the fitted Ni 2p profile shown in Fig. 4b, there are four species with two spin–orbit interactions and two vibrating satellite peaks (861.0 and 879.8 eV). The peak at a low binding energy of 855.3 eV is ascribed to Ni $2p_{3/2}$, while the peak at the high binding energy of 873.4 eV is attributed to Ni $2p_{1/2}$, which indicate the existence of nickel moieties in the +2 state.[57] In the S 2p spectrum (Fig. 4c), the broad S 2p is fitted into four peaks, while sulfate was formed by the oxidation of sulfur with a peak at 168.2 eV.[58] The peaks with binding energies at 161.2 and 161.9 eV are ascribed to the S $2p_{3/2}$ and S $2p_{1/2}$ orbits of divalent sulfides (S^{2-}), and the peaks at 163.1 and 164.2 eV indicate the presence of bridging S_2^{2-} in the CNS/N-rGO composite.[58] The calculated ratio of S_2^{2-}/S^{2-} is 3.254/1, which indicates that S_2^{2-} is the main component of CNS/N-rGO. Therefore, the CNS nanoparticles formed on the surface of rGO are mainly composed of CoS_2 and NiS_2, which is consistent with the XRD analysis results. The strong interaction between CNS and polysulfides is conducive to accelerate the redox reaction of polysulfides and enhance the cycle life of Li–S batteries. The N 1s XPS spectrum in Fig. 4d can be resolved into three peaks at 398.3, 400.5, and 402.3 eV, corresponding to pyridinic-N, pyrrolic-N, and quaternary-N, respectively. The doped nitrogen atom increases the polarity of the

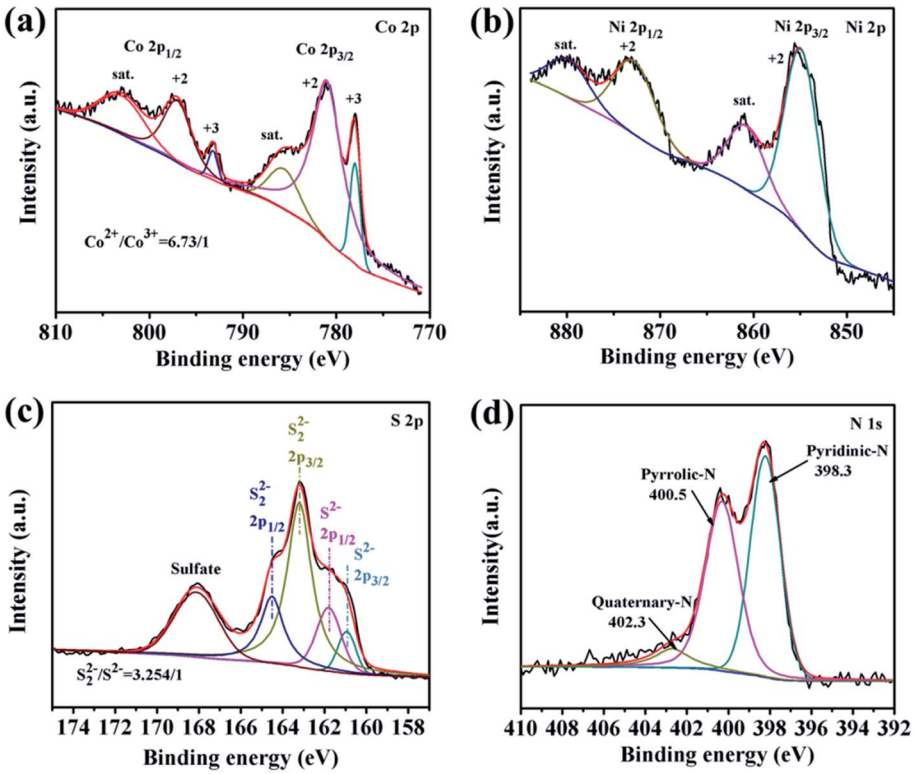

Fig. 4 XPS results for the CNS/N-rGO composite. (a) Co 2p spectra, (b) Ni 2p spectra, (c) S 2p spectra, and (d) N 1s spectra.

graphene surface, providing active adsorption sites for the adsorption of LiPSs, which is beneficial to improve the cycle stability of Li–S batteries.[43,52]

The microstructure of CNS/N-rGO was further studied by high-resolution transmission electron microscopy (HRTEM). The image at low magnification in Fig. 5a shows that rGO has a wavy and curved 2D morphology, and CNS nanoparticles can be seen adhering to rGO. The high-resolution TEM image (Fig. 5b) clearly shows that the size of the formed CNS particles is approximately 4–7 nm, and the CNS particle is encapsulated by 2–3 layers of rGO sheets. In addition, the corresponding element mappings (Fig. 5d–h) by EDS display that the elements of C, N, Co, Ni and S are evenly distributed in the whole composite. Thus, these results further demonstrate that N atoms and CNS particles were successfully deposited on the rGO nanosheets.

2.2. Electrochemical performance of Li–S batteries

A series of electrochemical measurements were performed using CNS/N-rGO/S as the active cathode material for Li–S batteries. The cyclic voltammetry (CV) plots of the CNS/N-rGO/S composite at a scan rate of 0.1 mV s^{-1} are demonstrated in Fig. 6a. During the discharge of the sulfur cathode, there are two distinct discharge platforms corresponding to the reduction peaks at ~2.30 V and ~2.00 V. The peak at 2.30 V is attributed to the conversion of S8 to high-order lithium polysulfide (Li_2S_x, $4 \leq x \leq 8$), while the peak at ~2.00 V corresponds to the high-order lithium polysulfide further reduced to insoluble Li_2S_2 and Li_2S.[55] During the charging process, partially overlapping strong oxidation peaks appear at 2.37 and 2.45 V due to the loss of electrons in Li_2S_2/Li_2S to form high-order lithium polysulfide, which was subsequently further oxidized to elemental sulfur.[19] The position of the two reduction peaks of CNS/N-rGO/S in the first cycle shifted because the redox process of the sulfur cathode has more stable sites after activation of the first charge/discharge cycle.[3,7] Notably, compared with the CV profiles of NiS_2/N-rGO/S and CoS_2/N-rGO/S (Fig. S1†), there is no significant change in the peak during the third and second cycles, indicating that the reduction of active sulfur of CNS/N-rGO/S is small and the CNS/N-rGO/S cathode possesses better electrochemical stability and reversibility.[46,59] Fig. 6b shows the galvanostatic charge–discharge profiles at 0.2C for the CNS/N-rGO/S, CNO/rGO/S and rGO/S cathodes. It can be observed that there are two discharge voltage plateaus at 2.30 V and 2.10 V, and one charge voltage plateau at ~2.25 V. Fig. S2(a)† shows the galvanostatic charge–discharge profiles at 0.2C for the NiS_2/N-rGO/S and CoS_2/N-rGO/S cathodes. The charge curves and discharge curves of NiS_2/N-rGO/S and CoS_2/N-rGO/S are consistent with their CV curves (Fig. S1†), and their capacity exhibited a significant downward trend. The initial discharge specific capacity of CNS/N-rGO/S reached 1115 mA h g^{-1} at 0.2C, and the discharge capacities of CNO/rGO/S, rGO/S, NiS_2/N-rGO/S and CoS_2/N-rGO/S were 1008 mA h g^{-1}, 926 mA h g^{-1}, 958 mA h g^{-1} and 989 mA h g^{-1}, respectively. Compared with rGO-S CNO/rGO/S, NiS_2/N-rGO/S and CoS_2/N-rGO/S, the CNS/N-rGO/S cathode exhibited a lower polarized voltage and higher specific capacity,

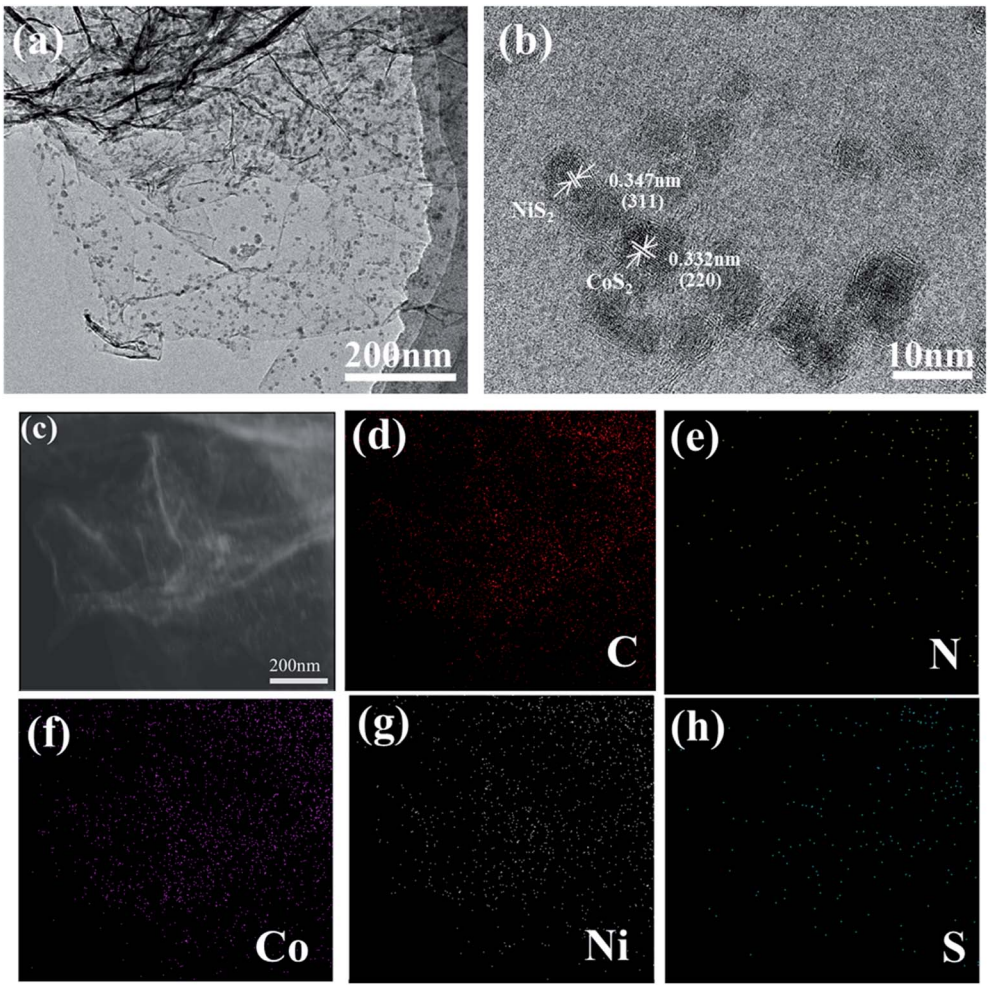

Fig. 5 (a) TEM and (b) HRTEM images of the CNS/N-rGO sample. (c) Dark-field STEM image of the CNS/N-rGO composite and the corresponding EDX elemental mappings of (d) C, (e) N, (f) Co, (g) Ni and (h) S.

indicating that it has faster redox reaction kinetics and increased utilization of sulfur.[60]

Fig. 6c displays the rate performance of the three cathodes at various rates ranging from 0.1 to 3C and the galvanostatic charge/discharge curves of the CNS/N-rGO/S cathode at various C rates (0.1–3C) are shown in Fig. 6d. CNS/N-rGO/S delivered a high discharge capacity of 1430, 1115, 961, 830, 725, and 622 mA h g^{-1} at the rates of 0.1, 0.2, 0.5, 1, 2, and 3C, respectively. When the rate was suddenly switched from 3C back to 0.1C, the original capacity was mostly recovered (1072 mA h g^{-1}), indicating that the CNS/N-rGO/S cathode has excellent reversible capacity at different rates. Compared with CNS/N-rGO/S, the CNO/rGO/S and rGO/S cathodes had lower discharge capacities at the same rates, especially at a high current rate of 3C, which is mainly caused by the shuttle of soluble lithium polysulfides.[52]

Fig. 6e shows the long cycle performance of the three cathodes at a current rate of 0.5C. The CNS/N-rGO/S cathode still delivered a specific capacity of 685 mA h g^{-1} after 300 cycles, which demonstrated a very low capacity decay rate of 0.075% per cycle and a high capacity retention rate of 78%. The specific capacity of CNO/rGO/S and rGO/S decreased from 815 and 757 mA h g^{-1} to 506 and 346 mA h g^{-1} after 300 cycles, respectively. The capacity attenuation rates of CNO/rGO/S and rGO/S in each cycle were 0.12% and 0.18%, respectively. Furthermore, the coulombic efficiency of CNS/N-rGO/S was higher than 98% after 300 cycles, and that of CNO/rGO/S was more than 96% after 300 cycles, while that of rGO/S was only about 91%. The reason for the low coulombic efficiency and poor cycling stability of the rGO/S cathode is that the surface of rGO is smooth and there are only a few adsorption sites for polysulfides; thus, it was impossible to capture the polysulfides produced during charging and discharging. Fig. S2(b)† shows the long cycle performance of the NiS_2/N-rGO/S and CoS_2/N-rGO cathodes at a current rate of 0.5C. The specific capacity of NiS_2/N-rGO/S and CoS_2/N-rGO/S decreased from 792 and 813 mA h g^{-1} to 461 and 558 mA h g^{-1} after 300 cycles, respectively. The capacity attenuation rates of NiS_2/N-rGO/S and CoS_2/N-rGO/S in each cycle were 0.14% and 0.11%, respectively. The coulombic efficiency of NiS_2/N-rGO/S and CoS_2/N-rGO/S was more than 96% after 300 cycles. Additionally, the CNS/N-rGO/S cathode had the highest specific capacity among the five cathodes over 300 cycles at 0.5C, which proves that CNS/N-

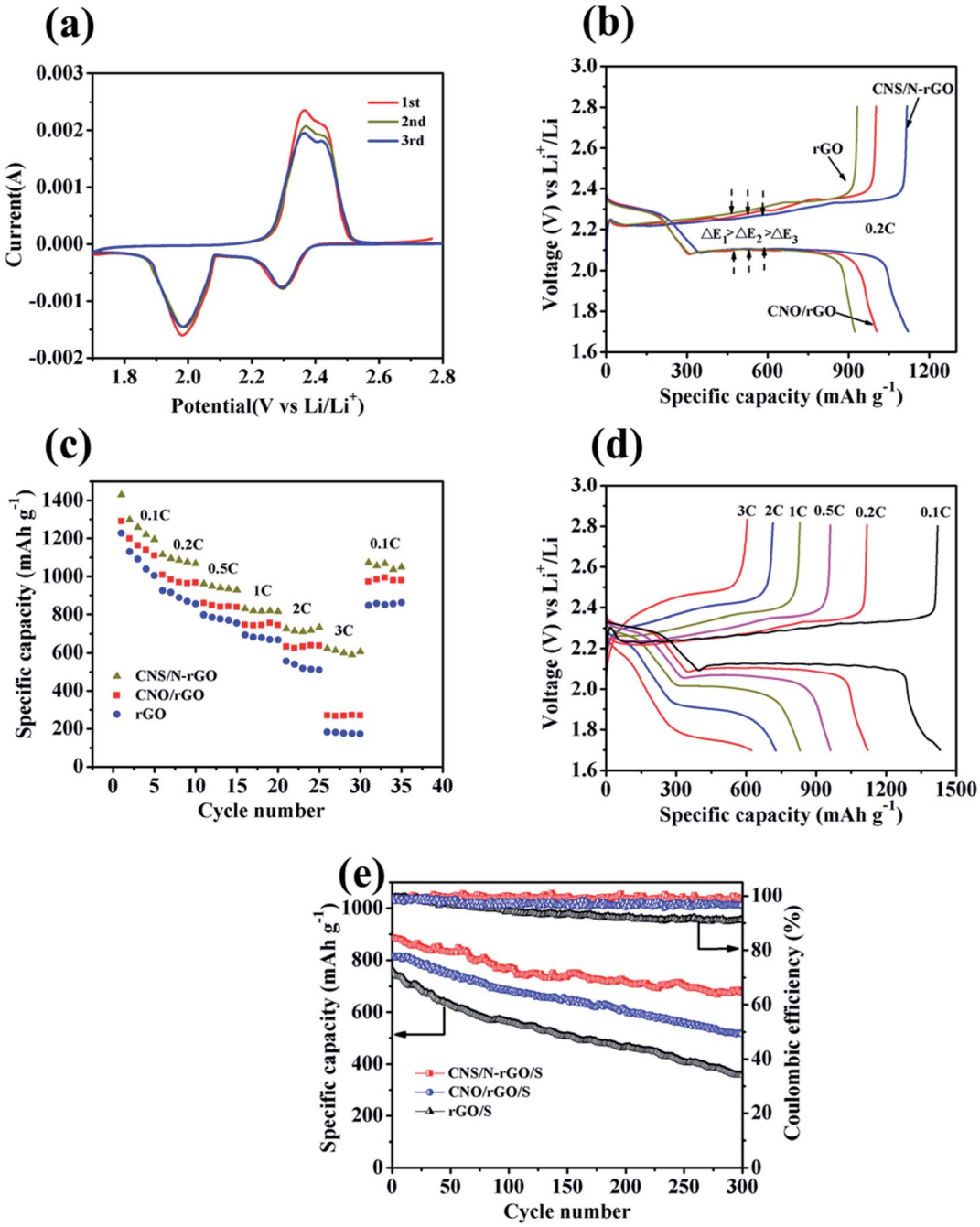

Fig. 6 (a) Cycle voltammograms of the CNS/N-rGO/S cathode at a scan rate of 0.1 mV s^{-1}. (b) Galvanostatic discharge/charge curves at 0.2C and (c) rate performance of the CNS/N-rGO/S, CNO/rGO/S and rGO/S cathodes at various rates (0.1–3C). (d) Typical galvanostatic discharge/charge profiles of the CNS/N-rGO/S cathode at different rates. (e) Cycling performance and Coulombic efficiency of the CNS/N-rGO/S, CNO/rGO/S and rGO/S cathodes at 0.5C for 300 cycles.

rGO can effectively restrain the notorious shuttle effect and improve the long-cycle performance.[9]

Long cycle stability is an important indicator for evaluating the life performance of Li–S batteries. Fig. 7a and b display the long-term cycling stability of the CNS/N-rGO/S cathode and its corresponding typical charge–discharge profiles at different cycles at 1C. The capacity of CNS/N-rGO/S cathode was attenuated from 766 to 526 mA h g^{-1} after 500 cycles, with an average coulombic efficiency of 98%, with the corresponding capacity decay rate of only 0.063% per cycle and the capacity retention rate of about 68.7%. In addition, compared with the cycle performance at 0.5C, the CNS/N-rGO/S cathode had better cycle stability and a lower capacity decay rate at 1C cycle. The SEM images of the electrode material after 500 cycles in Fig. 7c and d show that its 3D network structure underwent subtle changes, which maybe because of the presence of conductive agents and

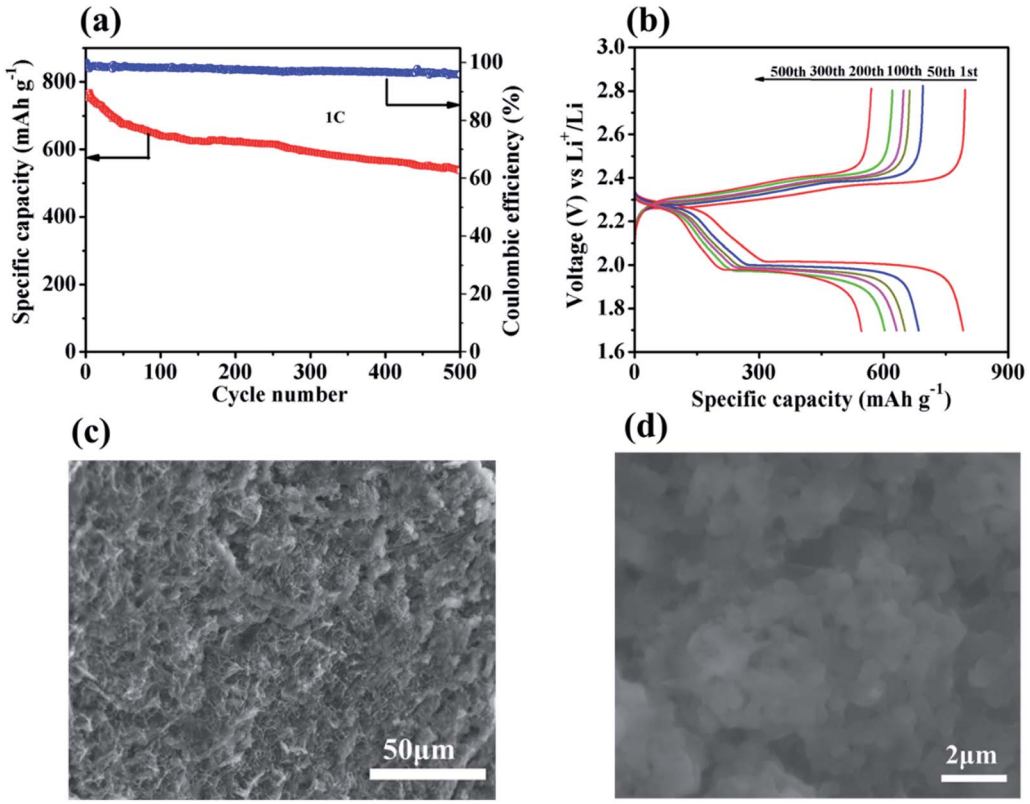

Fig. 7 (a) Cycling performance and (b) discharge–charge voltage profiles in different cycles of the CNS/N-rGO/S cathode at a current rate of 1C. (c) and (d) SEM images of CNS/N-rGO/S after 500 cycles.

coagulants, but the morphology of the electrode material did not change much. This proves the structural stability of the electrode material.

To further reveal the affinity of CNS/N-rGO to LiPSs, an absorption experiment was performed using Li_2S_6 as a representative polysulfide. The equivalent mass of rGO, CNO/rGO and CNS/N-rGO was separately added to a 2 mM Li_2S_6 solution in exactly the same amount and concentration. The absorption of LiPSs by the three sulfur host materials can be clearly distinguished in Fig. 8. After standing for 30 min after the addition of CNS/N-rGO, the solution changed from golden yellow to completely colorless because of the rapid and complete adsorption of Li_2S_6 by CNS/N-rGO. After standing for 2 h, the solution with CNO/rGO was clearly observed to change from golden yellow to light yellow, whereas the solution containing rGO still kept its golden yellow without any color change. In addition, we also carried out ultraviolet-visible absorption tests, as shown in Fig. 8. The experimental results show that CNS/N-rGO could quickly adsorb LiPSs formed during charging/discharging, and CNO/rGO could also slowly adsorb some of the LiPSs, while rGO has no adsorption effect. The Nyquist plots of the initial CNS/N-rGO/S and after 300 cycles at 0.5C are shown in Fig. S3.† The initial curve and the curve after 300 cycles are composed of two semicircles in the high and middle frequency area and a straight line in the low frequency area. In general, the semicircle in the high frequency region corresponds to the solid electrolyte interphase (SEI) layer resistance and the semicircle in the middle frequency region corresponds to the charge-transfer process.[61–63] Therefore, the electron transfer resistance of the material after the reaction was reduced quickly due to the formation of a stable interface, which yields a fast charge transfer, and thus enhances the redox kinetics.

To study whether the CNS/N-rGO composite can catalyze the redox reaction of polysulfides, the redox behavior of Li_2S_6 in three symmetrical cells was observed, as shown in Fig. 9a. It can

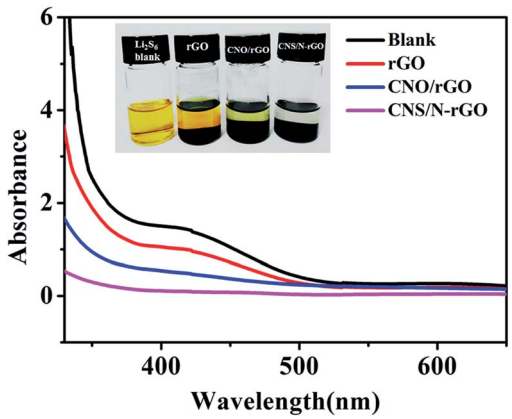

Fig. 8 Visualized adsorption test. UV-vis spectra of blank Li_2S_6 solution and Li_2S_6 solution with rGO, CNO/rGO and CNS/N-rGO after 2 h. The inset shows an optical image of the CNS/N-rGO, CNO/rGO and rGO materials soaked in the Li_2S_6 DME/DOL solution.

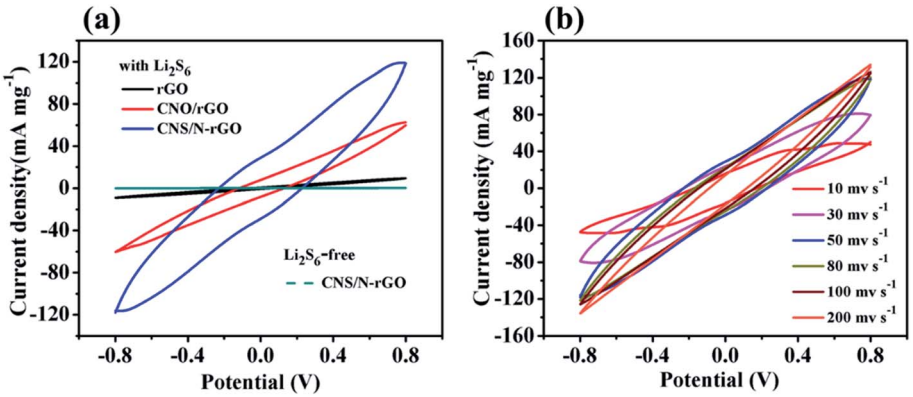

Fig. 9 (a) CV profiles of the symmetric cells using rGO, CNO/rGO and CNS/N-rGO as electrodes at 50 mV s^{-1} in the voltage window of −0.8 to 0.8 V. (b) CV curves of the symmetric CNS/N-rGO cell at scan rates ranging from 10 to 200 mV s^{-1}.

be clearly observed that the Li_2S_6-free symmetrical cell has only a small capacitive current, while the current density of Li_2S_6 in the CNS/N-rGO cell increased by an order of magnitude compared to that of the CNO/rGO cell, and the current density of Li_2S_6 in the CNO/rGO cell is much larger than that of the rGO cell, which indicates that the interaction between CNS/N-rGO and polysulfides not only statically exists but also dynamically accelerates the redox reaction of lithium polysulfide.[44,64] Fig. 9b shows the CV curves of the CNS/N-rGO cell at different scan rates, which have a similar shape and maintain good reversibility, even at a scan rate of up to 200 mV s^{-1}, indicating that the N and CNS particles in CNS/N-rGO greatly promote the kinetics of a series of polysulfide conversions.[64] The superior electrochemical performance of the CNS/N-rGO composite in Li–S batteries can be attributed to the following two aspects. (i) CNS nanoparticles and N on the surface of rGO can serve as effective sites for anchoring LiPSs. Both of them capture LiPSs by chemical adsorption, which enhances the ability to adsorb LiPSs and inhibits the diffusion of polysulfide. (ii) Encapsulation S with rGO nanosheets can effectively suppress the diffusion of polysulfides and decrease the loss of active sulfur materials, and the 3D network structure can provide channels for the diffusion of ions and the electrolyte and promote the rapid transfer of electrons and ions.

3. Conclusions

In summary, Co–Ni–S nanoparticles anchored on 3D N-doped reduced graphene aerogel were synthesized *via* a facile one-step hydrothermal method as a sulfur host material for lithium–sulfur batteries. The Co–Ni–S nanoparticles and N on the surface of rGO act as effective active adsorption sites for anchoring LiPSs, while the 3D network structure of graphene provides void space for the accommodation of sulfur and tunnels for the transport of ions and electrons. Consequently, the CNS/N-rGO composite displayed a high initial specific capacity of 1430 mA h g^{-1} at 0.1C, excellent rate performance and long cyclic stability. Furthermore, it exhibited long-term cycling stability and maintained a specific capacity of 526 mA h g^{-1} after 500 cycles at 1C. CNS/N-rGO as a sulfur host can promote the redox reaction kinetics process, and offer strong chemisorption for polysulfides, effectively inhibiting the shuttle effect of polysulfides to achieve a long cycle life in Li–S batteries.

Conflicts of interest

There are no conflicts to declare.

Acknowledgements

G.-P. D. acknowledges the National Natural Science Foundation of China (Grants 51762032 and 51462022) and the Natural Science Foundation Major Project of Jiangxi Province of China (Grant 20152ACB20012) for financial support of this research. The assistance of Dr Zhi-Qun Tian (HRTEM measurements) at Guangxi University and Dr A. S. Kumbhar (SEM and HRTEM measurements), CHANL at UNC Chapel Hill, is also greatly appreciated.

References

1 P. G. Bruce, S. A. Freunberger, L. J. Hardwick and J.-M. Tarascon, *Nat. Mater.*, 2012, **11**, 19–29.
2 J. B. Goodenough and K. S. Park, *J. Am. Chem. Soc.*, 2013, **135**, 1167–1176.
3 A. Manthiram, Y. Fu, S.-H. Chung, C. Zu and Y.-S. Su, *Chem. Rev.*, 2014, **114**, 11751–11787.
4 M. Yu, R. Li, Y. Tong, Y. Li, C. Li, J.-D. Hong and G. Shi, *J. Mater. Chem. A*, 2015, **3**, 9609–9615.
5 M. Liu, X. Qin, Y.-B. He, B. Li and F. Kang, *J. Mater. Chem. A*, 2017, **5**, 5222–5234.
6 R. Fang, S. Zhao, Z. Sun, D.-W. Wang, H.-M. Cheng and F. Li, *Adv. Mater.*, 2017, **29**, 1606823.
7 J. Jia, K. Wang, X. Zhang, X. Sun, H. Zhao and Y. Ma, *Chem. Mater.*, 2016, **28**, 7864–7871.
8 A. Manthiram, Y. Fu and Y.-S. Su, *Acc. Chem. Res.*, 2013, **46**, 125–1134.
9 W. Hua, Z. Yang, H. Nie, Z. Li, J. Yang, Z. Guo, C. Ruan, X. Chen and S. Huang, *ACS Nano*, 2017, **11**, 2209–2218.

10 Y. Wu, M. Gao, X. Li, Y. Liu and H. Pan, *J. Alloys Compd.*, 2014, **608**, 220–228.
11 Y.-S. Su and A. Manthiram, *Chem. Commun.*, 2012, **48**, 8817–8819.
12 Y. V. Mikhaylik and J. R. Akridge, *J. Electrochem. Soc.*, 2004, **151**, A1969–A1976.
13 N. Deng, W. Kang, Y. Liu, J. Ju, D. Wu, L. Li, B. S. Hassanb and B. Cheng, *J. Power Sources*, 2016, **331**, 132–155.
14 P. Zhu, J. Zang, J. Zhu, Y. Lu, C. Chen, M. Jiang, C. Yan, M. Dirican, R. K. Selvan, D. Kim and X. Zhang, *Carbon*, 2018, **126**, 594–600.
15 J. Song, M. L. Gordin, T. Xu, S. Chen, Z. Yu, H. Sohn, j. Lu, Y. Ren, Y. Duan and D. Wang, *Angew. Chem., Int. Ed.*, 2015, **127**, 4399–4403.
16 H. Lu, K. Zhang, Y. Yuan, F. Qin, Z. Zhang, Y. Lai and Y. Liu, *Electrochim. Acta*, 2015, **161**, 55–62.
17 J. Cao, C. Chen, Q. Zhao, N. Zhang, Q. Lu, X. Wang, Z. Niu and J. Chen, *Adv. Mater.*, 2016, **28**, 9629–9636.
18 Y. Son, J. S. Lee, Y. Son, J. H. Jang and J. Cho, *Adv. Energy Mater.*, 2015, **5**, 1500110.
19 G. Li, J. Sun, W. Hou, S. Jiang, Y. Huang and J. Geng, *Nat. Commun.*, 2016, **7**, 10601.
20 J. Song, Z. Yu, M. L. Gordin and D. Wang, *Nano Lett.*, 2016, **16**, 864–870.
21 G. He, X. L. Ji and L. Nazar, *Energy Environ. Sci.*, 2011, **4**, 2878–2883.
22 J. Schuster, G. He, B. Mandlmeier, T. Yim, K. T. Lee, T. Bein and L. F. Nazar, *Angew. Chem., Int. Ed.*, 2012, **51**, 3591–3595.
23 Y. J. Choi, K. W. Kim, H. J. Ahn and J. H. Ahn, *J. Alloys Compd.*, 2008, **449**, 313–316.
24 G. Y. Zheng, Y. Yang, J. J. Cha, S. S. Hong and Y. Cui, *Nano Lett.*, 2011, **11**, 4462–4467.
25 J. C. Guo, Y. H. Xu and C. S. Wang, *Nano Lett.*, 2011, **11**, 4288–4294.
26 Y. Hwa, H. K. Seo, J. M. Yuk and E. J. Cairns, *Nano Lett.*, 2017, **17**, 7086–7094.
27 F. Liu, Q. Xiao, H. B. Wu, F. Sun, X. Liu, F. Li, Z. Le, L. Shen, G. Wang, M. Cai and Y. Lu, *ACS Nano*, 2017, **11**, 2697–2705.
28 C. Wang, X. Wang, Y. Wang, J. Chen, H. Zhou and Y. Huang, *Nano Energy*, 2015, **11**, 678–686.
29 R. Chen, T. Zhao, J. Lu, F. Wu, L. Li, J. Chen, G. Tan, Y. Ye and K. Amine, *Nano Lett.*, 2013, **13**, 4642–4649.
30 M. Q. Zhao, Q. Zhang, J. Q. Huang, G. L. Tian, J. Q. Nie, H. J. Peng and F. Wei, *Nat. Commun.*, 2014, **5**, 3410.
31 C. Wang, X. Wang, Y. Yang, A. Kushima, J. Chen, Y. Huang and J. Li, *Nano Lett.*, 2015, **15**, 1796–1802.
32 Z. Wang, Y. Dong, H. Li, Z. Zhao, H. B. Wu, C. Hao, S. Liu, J. Qiu and X. W. Lou, *Nat. Commun.*, 2014, **5**, 5002.
33 J. He, G. Hartmann, M. Lee, G. S. Hwang, Y. Chen and A. Manthiram, *Energy Environ. Sci.*, 2019, **12**, 344–350.
34 G. Zhang, H. Peng, C. Zhao, X. Chen, L. Zhao, P. Li, J. Huang and Q. Zhang, *Angew. Chem., Int. Ed.*, 2018, **57**(51), 16732–16736.
35 Y. Tian, Y. Zhao, Y. Zhang, L. Ricardez-Sandoval, X. Wang and J. Li, *ACS Appl. Mater. Interfaces*, 2019, **11**(26), 23271–23279.
36 J. Jin, Z. Wen, G. Ma, Y. Lu, Y. Cui, M. Wu, X. Liang and X. Wu, *RSC Adv.*, 2013, **3**, 2558–2560.
37 C. Zhang, W. Lv, W. Zhang, X. Zheng, M. B. Wu, W. Wei, Y. Tao, Z. J. Li and Q. H. Yang, *Adv. Energy Mater.*, 2014, **4**, 1301565.
38 G. Zhou, L. C. Yin, D. W. Wang, L. Li, S. Pei, I. R. Gentle, F. Li and H. M. Cheng, *ACS Nano*, 2013, **7**, 5367–5375.
39 Y. Li, J. Fan, J. Zhang, J. Yang, R. Yuan, J. Chang, M. Zheng and Q. Dong, *ACS Nano*, 2017, **11**, 11417–11424.
40 L. Ji, M. Rao, H. Zheng, L. Zhang, Y. Li, W. Duan, J. Guo, E. J. Cairns and Y. Zhang, *J. Am. Chem. Soc.*, 2011, **133**, 18522–18525.
41 W. F. Li, M. N. Liu, J. Wang and Y. G. Zhang, *Acta Phys.-Chim. Sin.*, 2017, **33**, 165–182.
42 M. R. Sovizi, M. R. Yaftian and S. T. Seyyedin, *New J. Chem.*, 2017, **41**, 12589–12595.
43 C. Zheng, S. Niu, W. Lv, G. Zhou, J. Li, S. Fan, Y. Deng, Z. Pan, B. Li, F. Y. Kang and Q. H. Yang, *Nano Energy*, 2017, **33**, 306–312.
44 Z. Yuan, H. J. Peng, T. Z. Hou, J. Q. Huang, C. M. Chen, D. W. Wang, X. B. Cheng, F. Wei and Q. Zhang, *Nano Lett.*, 2016, **16**, 519–527.
45 Y. C. Qiu, W. F. Li, W. Zhao, G. Z. Li, Y. Hou, M. N. Liu, L. S. Zhou, F. M. Ye, H. F. Li, Z. H. Wei, S. H. Yang, W. H. Duan, Y. F. Ye, J. H. Guo and Y. G. Zhang, *Nano Lett.*, 2014, **14**, 4821–4827.
46 X. Cong, C. Cheng, Y. Liao, Y. Ye, C. Dong, H. Sun, X. Ji, W. Zhang, P. Fang, L. Miao and J. Jiang, *J. Phys. Chem. C*, 2015, **119**, 20864–20870.
47 X. Lu, Q. Zhang, J. Wang, S. Chen, J. Ge, Z. Liu, L. Wang, H. Ding, D. Gong, H. Yang, X. Yu, J. Zhu and B. Lu, *Chem. Eng. J.*, 2019, **358**, 955–961.
48 Y. Zhang, N. Wang, P. Xue, Y. Liu, B. Tang, Z. Bai and S. Dou, *Chem. Eng. J.*, 2018, **343**, 512–519.
49 J. He, Y. Chen and A. Manthiram, *iScience*, 2018, **4**, 36–43.
50 H. S. Han, K. M. Kim, H. Choi, G. Ali, K. Y. Chung, Y. R. Hong, J. Choi, J. Kwon, S. W. Lee, J. W. Lee, J. H. Ryu, T. Song and S. Mhin, *ACS Catal.*, 2018, **8**, 4091–4102.
51 G. He, M. Qiao, W. Li, Y. Lu, T. Zhao, R. Zou, B. Li, J. A. Darr, J. Hu, M. M. Titirici and I. P. Parkin, *Adv. Sci.*, 2017, **4**, 1600214.
52 Y. Gong, C. Fu, G. Zhang, H. Zhou and Y. Kuang, *Electrochim. Acta*, 2017, **256**, 1–9.
53 Z. Li, Y. Jiang, L. Yuan, Z. Yi, C. Wu, Y. Liu, P. Strasser and Y. Huang, *ACS Nano*, 2014, **8**, 9295–9303.
54 V. Sridhar and H. Park, *J. Alloys Compd.*, 2018, **764**, 490–497.
55 R. Fang, S. Zhao, S. Pei, X. Qian, P. X. Hou, H. M. Cheng, C. Liu and F. Li, *ACS Nano*, 2016, **10**, 8676–8682.
56 X. Sun, H. Huang, C. Wang, Y. Liu, T. L. Hu and X. H. Bu, *ChemElectroChem*, 2018, **5**, 3639–3644.
57 H. Li, M. Wang, Y. Wei and F. Long, *J. Colloid Interface Sci.*, 2019, **534**, 343–349.
58 P. Wang, X. Zhang, J. Zhang, S. Wan, S. Guo, G. Lu, J. Yao and X. Huang, *Nat. Commun.*, 2017, **8**, 14580.
59 H. Li, L. Sun, Z. Wang, Y. Zhang, T. Tan, G. Wang and Z. Bakenov, *Nanomaterials*, 2018, **8**, 69–81.

60 G. Zhou, E. Paek, G. S. Hwang and A. Manthiram, *Nat. Commun.*, 2015, **6**, 7760.
61 J. Yao, Y. Gong, S. Yang, P. Xiao, Y. Zhang, K. Keyshar, G. Ye, S. Ozden, R. Vajtai and P. M. Ajayan, *ACS Appl. Mater. Interfaces*, 2014, **6**, 20414–20422.
62 Z. Deng, Z. Zhang, Y. Lai, J. Liu, J. Li and Y. Liu, *J. Electrochem. Soc.*, 2013, **160**, A553–A558.
63 G. P. Hao, C. Tang, E. Zhang, P. Zhai, J. Yin, W. Zhu, Q. Zhang and S. Kaskel, *Adv. Mater.*, 2017, **29**, 1702829.
64 L. Zhang, Z. Chen, N. Dongfang, M. X. Li, C. Z. Diao, Q. S. Wu, X. Chi, P. L. Jiang, Z. D. Zhao, L. Dong, R. C. Che, K. P. Loh and H. B. Lu, *Adv. Energy Mater.*, 2018, **8**, 1802431.